Applied Ocean Research 166 (2026) 104892

Contents lists available at ScienceDirect

Applied Ocean Research

journal homepage: www.elsevier.com/locate/apor

Research paper

Numerical modelling of air-induced drag reduction allowing the transition between bubbly, air layer and mixed regimes

Benjamin Krull [a,*], Kasper Bilde [b], Christian Kringel [b,d], Richard Meller [a], Victor Molbak [d], Georgios Papaioannou [c], Fabian Schlegel [a], Matej Tekavčič [e], Filotas Tziaros [c]

[a] Helmholtz-Zentrum Dresden-Rossendorf, Dresden, Germany
[b] Alfa Laval Aalborg, Aalborg, Denmark
[c] Alfa Laval Rotterdam, Rotterdam, Netherlands
[d] Aalborg University, Aalborg, Denmark
[e] Jožef Stefan Institute, Ljubljana, Slovenia

ARTICLE INFO

Keywords:
Morphology-adaptive method
Bubbly flow
Gas injection
Air layer
Air lubrication
Drag reduction
Ship hull

ABSTRACT

Air lubrication can reduce the frictional resistance of ships, leading to significant fuel cost savings. However, the performance of air lubrication systems varies considerably, depending on the operating conditions. Complex gas morphologies play a crucial role here but are difficult to predict. Such a variety of morphologies (bubbly flow, air layers, or mixed regimes) requires morphology-adaptive methods, such as MultiMorph. This method allows for multiple morphologies of a given phase, including the transfer between them. The injection of gas can result in air bubbles, air layers, or a mixed regime, based on local transfer mechanisms. The ability to predict these morphologies is a distinctive feature of this method. Alternative methods prescribe a specific regime *a priori*, and do not allow a transition. To assess the suitability of MultiMorph for air lubrication problems, two geometries with different complexities are considered. The first test validates the method against flat plate experiments. Various water velocity and gas flow rate combinations were considered to investigate their influence on gas morphology and the associated drag reduction. The second case features a three-dimensional ship hull geometry with two bubble injectors to test the applicability of the method to a more complex scenario, including a curved geometry. The method performs well in both test cases and qualifies as a useful tool for numerical investigations of air lubrication phenomena.

1. Introduction

Skin friction causes a large portion of the energy consumption of water vessels (Thill et al., 2005). The contribution to the overall resistance is particularly high at low Froude numbers, computed from the ship velocity U, gravitational constant g, and length of the ship L_{ship}:

$$\mathrm{Fr} = \frac{U}{\sqrt{g L_{\mathrm{ship}}}} \ . \tag{1}$$

The value of $Fr \approx 0.2$ is typical for large ships, i.e. the regime in which the total loss is mainly caused by friction is very common. Air lubrication devices aim to reduce the frictional resistance by injecting gas beneath the ship hull. This improves the energy efficiency of maritime transport. In the literature, fuel cost savings of up to 8% (Fotopoulos and Margaris, 2020) or even 12% (Mizokami et al., 2010; Jang et al., 2014) have been reported. However, the effectiveness of air lubrication systems is strongly influenced by the air injection method and ship operating conditions (Giernalczyk and Kaminski, 2021). Under certain circumstances, the injection of air can have the opposite effect: it may cause a drag increase instead of a drag decrease (Kato et al., 1998; Murai, 2014). Drag reduction is typically measured by the normalized wall shear stress difference resulting from the injected air (Elbing et al., 2008):

$$\mathrm{DR} = \frac{\tau_{\mathrm{w,\ water\ only}} - \tau_{\mathrm{w,\ gas\ injection}}}{\tau_{\mathrm{w,\ water\ only}}} \ . \tag{2}$$

The wall-shear stress is defined as

$$\tau_{\mathrm{w}} = \mathbf{n} \cdot 2\mu \mathbf{S} \cdot \mathbf{e}_{\mathrm{x}} \ , \tag{3}$$

where $\mathbf{n}$ is the wall-normal, $\mathbf{S}$ is the symmetric part of the strain rate tensor, and x is assumed to be the main flow direction. The wall shear stress is a consequence of the local velocity gradients and local (effective) viscosity. The reduction in wall shear stress is strongly

---

* Corresponding author.
E-mail address: b.krull@hzdr.de (B. Krull).

https://doi.org/10.1016/j.apor.2025.104892
Received 28 October 2024; Received in revised form 8 December 2025; Accepted 9 December 2025

influenced by the occurring gas-liquid patterns beneath the hull. Three drag reduction regimes have been reported in the literature (Mäkiharju et al., 2012):

1. bubble drag reduction (BDR),
2. air layer drag reduction (ALDR), and
3. transitional regime.

Whether the injected bubbles persist (BDR) or form a layer of gas (ALDR) has direct implications on the drag reduction efficiency. The effect of injected bubbles (BDR) on turbulence is not decisive (Guin et al., 1996), whereas the effect on the effective viscosity plays an important role (Legner, 1984). The formation of an air layer is more likely for a low water velocity (low vessel velocity) combined with a high gas injection rate. For the ALDR, the drag reduction is explained by the fact that air causes less skin friction on the hull. The transitional regime represents a mixed state between the BDR and ALDR. This typically exists only within a narrow parameter range (Elbing et al., 2008). Drag reduction concepts based on geometric cavities also exist (Ceccio, 2010) but are not considered in the present work. An overview of air lubrication mechanisms is provided in Wang et al. (2022). Air lubrication systems hold promise as energy-saving technologies, but further research is needed to optimize their effectiveness under specific operating conditions and ship designs.

An overview of the research progress was presented in An et al. (2022). Experimental measurements have focused on flat plates (Elbing et al., 2008; Jang et al., 2014) and ship models (Jang et al., 2014; Park and Lee, 2018; Zhao et al., 2020). Numerical attempts have investigated either the bubbly regime (Zhao et al., 2020) or the air layer regime (Zhao et al., 2020; Kim and Park, 2021) using two-fluid, mixture, or volume-of-fluid methods, but not both in combination. To select the most suitable of these methods for a specific practical problem, the morphology must be known beforehand, that is, the user is forced to prescribe either bubbles or air layers. This is a disadvantage because information regarding the morphology is usually not available *a priori* in applications of practical relevance. Recent reviews have not mentioned methods that can predict the morphology of the injected gas (Chillemi et al., 2024). The present work attempts to overcome this limitation by relying on a framework that captures both bubbly and layered gas morphologies, including the transition between the two.

2. Numerical model

Established numerical methods prescribe the morphology of the gas phase, which means that the flow regime must be known in advance (An et al., 2022; Chillemi et al., 2024). They assume either a bubbly regime (and rely on the classical Euler-Euler method (Kunz et al., 2006; Mohanarangam et al., 2009; Qin et al., 2017) or the existence of a continuous air layer (and rely on the volume-of-fluid method or similar approaches (Kim et al., 2020; Kim and Park, 2021). Mixed regimes or changes in morphology over time cannot be captured. This is problematic for underwater air lubrication systems, because the morphology of a given configuration is usually unknown and is expected to evolve dynamically. Such requirements necessitate the development of morphology-adaptive techniques. They can model coexisting morphologies, including the transition from one morphology to another. The morphology type is part of the numerical prediction and is not predefined by the user.

The present work assesses the capability of the morphology-adaptive MultiMorph method (Schlegel et al., 2023) to predict phenomena related to air lubrication. This method is particularly suitable because it allows a) the coexistence of multiple morphologies and b) bidirectional transitions between these morphologies.

MultiMorph represents each morphology by a dedicated numerical phase k, each described by the phase-averaged RANS equations balancing mass and momentum:

$$\frac{\partial \alpha_k \rho_k}{\partial t} + \nabla \cdot (\alpha_k \rho_k \mathbf{u}_k) = \Gamma_k \,, \tag{4}$$

$$\frac{\partial \alpha_k \rho_k \mathbf{u}_k}{\partial t} + \nabla \cdot (\alpha_k \rho_k \mathbf{u}_k \mathbf{u}_k) = -\alpha_k \nabla p + \nabla \cdot (2 \alpha_k \mu_{k,\mathrm{eff}} \mathbf{S}_k) + \alpha_k \rho_k \mathbf{g} + \mathbf{f}_k + \mathbf{\Gamma}'_k \,, \tag{5}$$

$$\mathbf{f}_k = \sum_{l \neq k} \mathbf{f}_{kl}, \quad \Gamma_k = \sum_{l \neq k} \Gamma_{kl}, \quad \mathbf{\Gamma}'_k = \sum_{l \neq k} \Gamma_{kl} \mathbf{u}_{kl} \,. \tag{6}$$

Here, α is the phase fraction, ρ is the phase density, $\mathbf{u}$ is the phase velocity, t is the time, p is the shared pressure, $\mathbf{S}$ is, like above, the symmetric part of the strain rate tensor, $\mathbf{g}$ is the gravitational acceleration, $\mathbf{f}$ are the interfacial closure forces and surface tension effects. The mass transfer rate Γ_{kl} is positive if α_k is produced by reducing α_l and negative in the reverse case (which implies $\Gamma_{kl} = -\Gamma_{lk}$). These transfers result in the source terms Γ and $\mathbf{\Gamma}'$ for mass and momentum, respectively. The mass transfer velocity $\mathbf{u}_{kl}$ is equal to the velocity of the reduced phase. The momentum transfer terms also cancel out each other ($\mathbf{f}_{kl} = -\mathbf{f}_{lk}$). Turbulence is considered via the k-ω SST model (Menter, 2009), including wall functions for turbulent quantities (Rzehak and Kriebitzsch, 2015). The turbulence for the disperse gas was neglected, and dampening was applied on the continuous gas side (Tekavčič et al., 2021). A model for bubble-induced turbulence (Ma et al., 2017) was also activated (see the discussion of disperse phase modelling below).

To capture the air lubrication phenomenon, the following morphologies were considered in the numerical solver: continuous water (α_{water}), disperse air (α_{aird}), and continuous air (α_{airc}). The method allows the morphology to be adapted according to the local conditions based on geometrical reasoning. The transition of disperse air to continuous air (bubbles forming an air layer) is activated as soon as the local fraction of air exceeds the densest sphere packing limit (Schlegel et al., 2023). The transfer $\alpha_{\mathrm{aird}} \rightarrow \alpha_{\mathrm{airc}}$ is calculated according to:

$$\Gamma_{\mathrm{airc,aird}} = \rho_{\mathrm{air}} \frac{\sqrt{\alpha_{\mathrm{aird}}}}{\tau} \quad \text{while} \quad \alpha_{\mathrm{aird}} + \alpha_{\mathrm{airc}} \geq 0.74 \,. \tag{7}$$

The inequality condition ensures that the process runs continuously, potentially until no disperse material remains. In the reverse process, the transition of continuous air to disperse air (disintegration of an air layer into bubbles) is induced by a threshold undershoot, protecting the resolved interfacial regions (Meller et al., 2024). The transfer $\alpha_{\mathrm{airc}} \rightarrow \alpha_{\mathrm{aird}}$ is computed from:

$$\Gamma_{\mathrm{aird,airc}} = \rho_{\mathrm{air}} \frac{\sqrt{\alpha_{\mathrm{airc}}}}{\tau} \quad \text{while} \quad \alpha_{\mathrm{airc}} + \alpha_{\mathrm{water}} > 0.5 \quad \text{and} \quad \alpha_{\mathrm{airc}} < \alpha_{\mathrm{water}} \,, \tag{8}$$

provided that no interface is locally present. The conditions on the right-hand side ensure the existence of sufficient continuous material and that continuous air is only converted if it does not dominate locally. The formula for the mass transfer rate, $\rho_k \sqrt{\alpha_k}/\tau$, is identical in both the forward and backward directions. The time scale τ is a parameter selected to be independent of the selected discrete time step size to allow the algorithm to converge with decreasing time step sizes. Throughout the present work, the time scale was set to $\tau = 0.01\,\mathrm{s}$, which describes a relatively fast transfer and has proven to be a good choice in various air–water simulations. Note that these geometrical transfers must be distinguished from empirical transfer models, which are based on the local flow parameters obtained from specific experimental observations. There is no mass transfer between air and water (no phase change):

$$\Gamma_{\mathrm{aird,water}} = \Gamma_{\mathrm{airc,water}} = 0 \tag{9}$$

Non-zero interfacial forces $\mathbf{f}$ realize momentum coupling. The coupling of disperse air with continuous water accounts for drag, lift, virtual mass, wall effects, and turbulent dispersion as follows:

$$\mathbf{f}_{\mathrm{aird,water}} = \mathbf{f}^{\mathrm{drag}}_{\mathrm{aird,water}} + \mathbf{f}^{\mathrm{lift}}_{\mathrm{aird,water}} + \mathbf{f}^{\mathrm{VM}}_{\mathrm{aird,water}} + \mathbf{f}^{\mathrm{TD}}_{\mathrm{aird,water}} \tag{10}$$

These forces were chosen according to the Baseline model by HZDR, which defines a set of validated force formulations (Hänsch et al., 2021; Lehnigk et al., 2023). Note that the Baseline model also includes the effect of bubble-induced turbulence (Ma et al., 2017), which is considered here. This creates an important feedback loop because the bubbles react to the increased turbulence level according to the effect of turbulent dispersion. The coupling between two continuous phases is based on surface tension (implemented according to Brackbill et al. (1992)) and the drag force formulation proposed by Strubelj and Tiselj (2011):

$$\mathbf{f}_{\mathrm{airc,water}} = \mathbf{f}^{\sigma}_{\mathrm{airc,water}} + \mathbf{f}^{\mathrm{drag}}_{\mathrm{airc,water}}$$

$$\text{with} \quad \mathbf{f}^{\mathrm{drag}}_{\mathrm{airc,water}} = \frac{C\,\alpha_{\mathrm{airc}}\alpha_{\mathrm{water}}\,\rho_{\mathrm{airc,water}}}{\Delta t}\left(\mathbf{u}_{\mathrm{water}} - \mathbf{u}_{\mathrm{airc}}\right)\,, \tag{11}$$

where Δt denotes the time step size and $\rho_{\mathrm{airc,water}}$ refers to the phase-average density. This drag force equalizes the phase velocities. It requires a large dimensionless factor C, which is set to 10^8. To keep the problem numerically well defined, the coupling between disperse air and continuous air needs to be defined. This is achieved by introducing the artificial coupling force

$$\mathbf{f}_{\mathrm{aird,airc}} = K\left(\mathbf{u}_{\mathrm{airc}} - \mathbf{u}_{\mathrm{aird}}\right)\,, \tag{12}$$

which is applied only when the volume fraction of the disperse gas is below the residual value. The constant K is set to $1 \cdot 10^{-4}\,\mathrm{kg\,m^{-3}\,s^{-1}}$.

The coupling procedure allows a velocity difference between the disperse and continuous phases (interfacial slip) but matches the velocities of the tightly coupled continuous phases (no slip). This behaviour ensures that the method in use contains the classical algebraic volume-of-fluid method as an edge case.

The MultiMorph method has been validated (Meller et al., 2021; Tekavčič et al., 2021) and applied to various cases of different types, for example, to model a gas-liquid separator (Yin et al., 2023), droplet entrainment in annular flow (Wang et al., 2023), and a distillation column tray (Wiedemann et al., 2023). The solver is part of the Multiphase Code Repository by HZDR for OpenFOAM Foundation software and publicly available (Schlegel et al., 2024).

The wall-shear stress is computed according to

$$\tau_{\mathrm{w}} \approx \tau_{\mathrm{w,water}} = \mathbf{n} \cdot 2\alpha_{\mathrm{water}}\mu_{\mathrm{water,eff}}\mathbf{S}_{\mathrm{water}} \cdot \mathbf{e}_{\mathrm{x}}\,. \tag{13}$$

It is computed from the effective viscosity, i.e. from the resolved stress and the modelled turbulent stress. It is sufficient to consider the water-induced shear, as the air-induced proportion of the shear stress is negligible.

3. Validation against experimental results for a flat plate

3.1. Case description

It was ensured that the MultiMorph model can predict the air lubrication phenomenon. This was done by performing a comparison with generic quasi-2D experiments by Elbing et al. (2008). The authors considered a flat plate at different free stream velocities and gas injection rates and varied the injection method.

The computational setup is illustrated in Fig. 1. It is two-dimensional, with length $L_0 + L$ and vertical depth D. Therefore, spanwise gradients are not captured. The inlet velocity was set constant according to the free stream velocity U, assuming a certain turbulence intensity I_0. The upper wall allowed slip only for disperse air (bubbles). The gas was injected via mass point sources at a constant mass flow rate computed from q. Six mass point sources were equally distributed along a vertical line, with one millimeter distance, with the closest placed directly on the wall. The injected gas was assumed to be disperse with a constant diameter d_{b}, approximated from the bubble size distribution reported by Elbing et al. (2008). The chosen diameter is comparatively large, motivated by the definition of the Sauter mean diameter, which tends to be closer to the larger diameters of a given distribution. The robustness of the results with respect to the choice of the bubble diameter was investigated in a separate study (Section 3.5). The momentum of the injected gas was neglected. A fixed mean pressure boundary condition was applied to the outflow to ensure a smooth outflow of a potential air layer (continuous gas). The computational domain is resolved with $N_x \times N_y$ cells equidistantly in the horizontal direction and gradually refined in the vertical direction towards the wall. The refinement was applied to the upper 20% of the domain containing 35% of the cells with a grading factor of 0.2, resulting in a wall-nearest cell layer thickness of approximately $1\,\mathrm{mm}$. The time step was adjusted according to the global Courant number limit of 0.4. The simulations were performed until the integral drag value converged, which was typically the case after a few seconds. The setup is publicly available as part of the Multiphase Cases Repository by HZDR for OpenFOAM Foundation Software (Hänsch et al., 2024).

Table 1
Setup parameters for the flat plate case.

L_0	L	D	d_b	I_0	(N_x, N_y)
$2\,\mathrm{m}$	$10\,\mathrm{m}$	$0.5\,\mathrm{m}$	$0.3\,\mathrm{mm}$	5%	$(120, 80)$

The values of the aforementioned parameters are listed in Table 1. The values for the free stream velocity U and the gas flow rate per unit width q were varied, as described in the following sections.

3.2. Bubble drag reduction

The first test compared the drag reduction along the plate for a bubbly regime (no air layer should be created in the simulation). The free stream velocity $U = 13.3\,\mathrm{m\,s^{-1}}$ was considered together with the gas flow rate $q = 0.05\,\mathrm{m^2\,s^{-1}}$. The results are presented in Fig. 2 together with the experimental results (taken from Fig. 8 in Elbing et al. (2008)). The gas phase remained disperse, and the bubbles caused drag reduction with a peak close to the inlet. Some disperse material is converted into a continuous state immediately after injection, which disintegrates immediately. Note that the presence of gas slightly upstream of the injection point is a numerical artifact caused by the coarse resolution in the streamwise direction. The model's predictions are consistent with the experimental observations. The distribution of the drag reduction was also predicted quite well, decreasing downstream in a very similar manner as in the experiments.

3.3. Air layer drag reduction

The second test compared the drag reduction along the plate for an air layer regime (the injected bubbles were expected to form a film). The free stream velocity is the same as before ($U = 13.3\,\mathrm{m\,s^{-1}}$) but combined with a higher gas flow rate of $q = 0.08\,\mathrm{m^2\,s^{-1}}$. The results are presented in Fig. 3 together with the experimental results (again taken from Fig. 8 in Elbing et al., 2008). The experimentalists reported lower reduction values measured for the slot injection method. The underlying mechanisms are not fully understood and the differences lie within the uncertainty of the measurements (Section 3.2.5, Elbing et al., 2008). The model predicts the morphology and drag reduction in very good agreement with the porous plate injection experiments. This is plausible because the current setup injects disperse bubbles rather than continuous air. The injected disperse gas immediately formed a continuous air layer, leading to significant drag reduction.

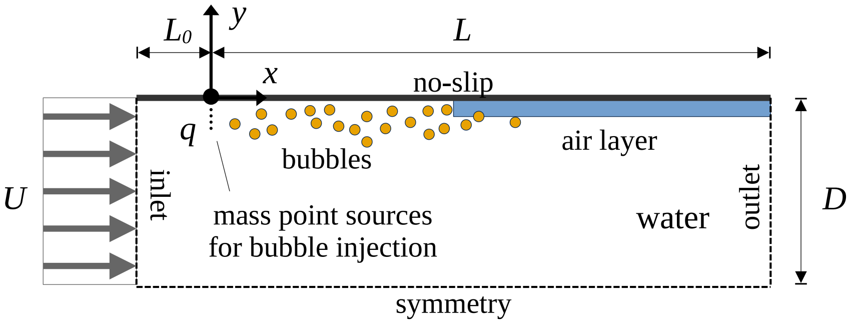

Fig. 1. Sketch of the two-dimensional computational setup for the flat plate case.

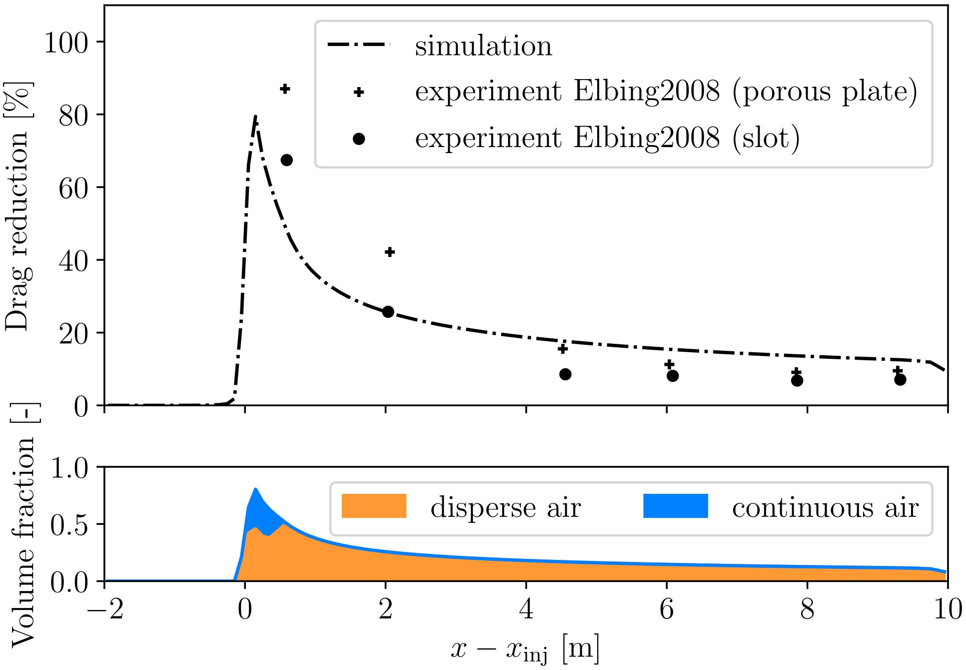

Fig. 2. Wall-near gas volume fraction (bottom, coloured area represents volume fraction) and drag reduction (top) in the flat plate case obtained for a free stream velocity of $U = 13.3\,\text{m}\,\text{s}^{-1}$ and a gas flow rate of $q = 0.05\,\text{m}^2\,\text{s}^{-1}$. Drag reduction is dominated by bubbles.

3.4. *Transitional regime*

The transitional regime is observed only in a very narrow range of parameters (Elbing et al., 2008). The regime change from bubbly to air-layer-dominated flow occurs suddenly and is difficult to observe experimentally. A discussion of the scaling of these transitional effects can be found in Elbing et al. (2013). In the transitional regime, drag reduction values between 20% and 80% are expected for the current configuration, as observed in the experiments at a lower free stream velocity of $U = 6.7\,\text{m}\,\text{s}^{-1}$ with gas flow rates $q = 0.014\,\text{m}^2\,\text{s}^{-1}$ and $q = 0.026\,\text{m}^2\,\text{s}^{-1}$, respectively (see Fig. 7 in Elbing et al. (2008)). The numerical results for both operation points are shown in Fig. 4. The model reproduced the morphologies in accordance with the experiments, reproducing a bubble-dominated regime for the lower gas flow rate ($q = 0.014\,\text{m}^2\,\text{s}^{-1}$) and an air layer dominated regime for the higher gas flow rate ($q = 0.026\,\text{m}^2\,\text{s}^{-1}$). For the lower gas flow rate, the drag reduction is underestimated. The drag reduction for the air layer regime is in qualitative accordance with the experimental data, given that the experimental results differ significantly depending on the injection method. The expected intermediate values for the drag reduction were not reproduced very well. The transition range observed in the experiments collapsed to a transition point: This transition point is investigated systematically using the present method and found to be between the gas flow rate of $q = 0.019\,\text{m}^2\,\text{s}^{-1}$ (still bubble-dominated) and $q = 0.020\,\text{m}^2\,\text{s}^{-1}$ (air-layer-dominated). This value lies within the transition range in the experiments (see Fig. 23 in Elbing et al. (2008)). It is expected that the present generic setup inherits artificially increased stability: three-dimensional effects are not captured in the present two-dimensional setup, but may play a decisive role here. Further reasons for the observed deviations are conceivable. For example, an overestimation of the turbulence level could lead to an increase in turbulent dispersion, pushing the bubbles away from the wall, which could hinder the formation of an air layer. Given the simplicity of the setup, the transition was predicted qualitatively.

3.5. *Uncertainties and sensitivity*

Note the following remarks on the uncertainties contained in the reference data and the influence of the physical assumptions and approximations in the numerical setup.

Uncertainties in the experiment. The authors of Elbing et al. (2008) describe the following uncertainties: They observed a significant change

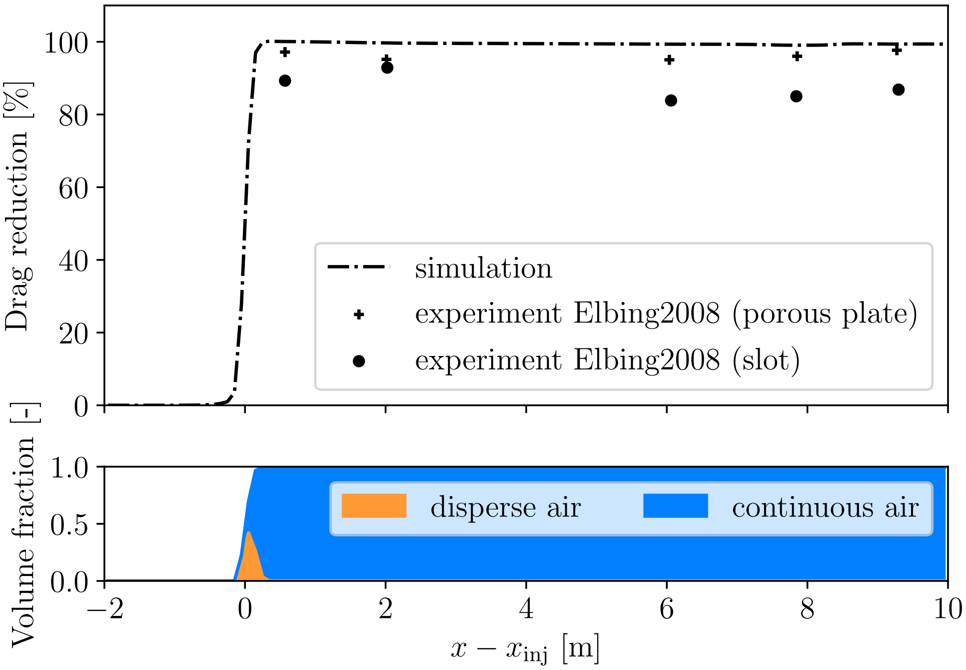

Fig. 3. Wall-near gas volume fraction (bottom, coloured area represents volume fraction) and drag reduction (top) in the flat plate case obtained for a free stream velocity of $U = 13.3\,\mathrm{m\,s^{-1}}$ and a gas flow rate of $q = 0.08\,\mathrm{m^2\,s^{-1}}$. Drag reduction is dominated by an air layer.

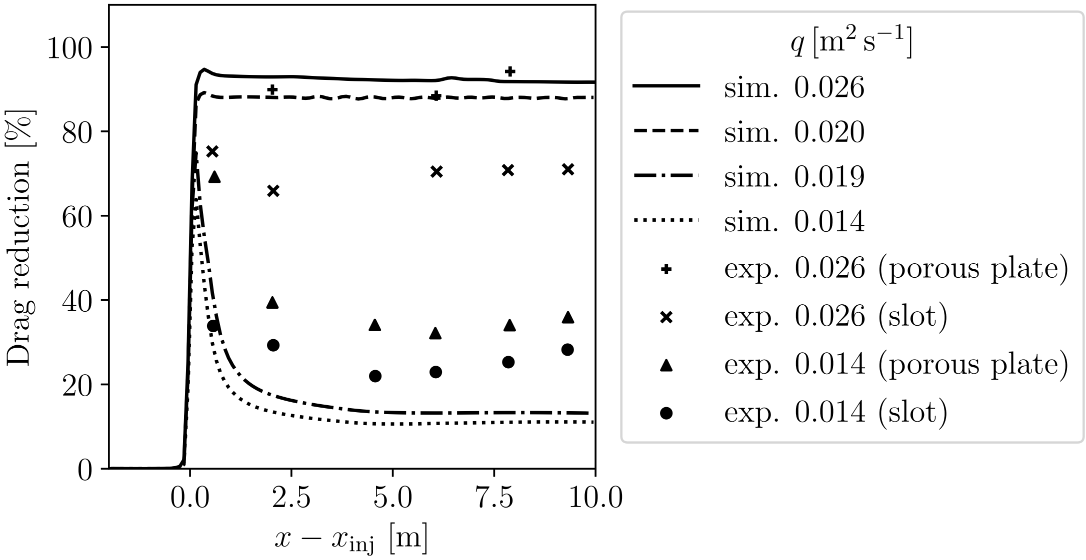

Fig. 4. Drag reduction for operating points in the transitional regime (free stream velocity fixed to $U = 6.7\,\mathrm{m\,s^{-1}}$, gas flow rate varied) in the flat plate case. The regime change occurs between the gas flow rate $q = 0.019\,\mathrm{m^2\,s^{-1}}$ and $q = 0.020\,\mathrm{m^2\,s^{-1}}$.

in the volume flow rate over time, forcing them to segment the measurements into 0.5 s intervals. They reported a ±95% confidence interval for the bubble imaging system and the qualitative characteristics of the electrical impedance probe measurements of near-wall void fractions above 50%. For the skin friction measurements, they reported an uncertainty of ±5%. The drag reduction value is the ratio of two skin friction values, which implies an error band of approximately ±10%.

Turbulence. The turbulence intensity at the inlet was set to $I_0 = 5\%$, which is a common choice if no information is available. This value has a direct effect on the strength of the turbulent dispersion: a high turbulence intensity pushes the bubbles away from the wall, making the formation of an air layer less likely. This underlines the importance of the turbulence modelling aspects of the setup: bubble-induced turbulence (Ma et al., 2017), turbulence damping on the continuous gas side (Tekavčič et al., 2021), and the choice of turbulent dispersion closure (Burns et al., 2004) play an important role (selected according to the HZDR Baseline strategy mentioned in Sec. 2). The results were robust against small variations in the turbulence intensity of the free stream inlet (±5%).

Injection method. Elbing et al. (2008) report a minor influence of the injection method. The differences between porous plate injection and slot injection were within the measurement uncertainty (Elbing et al., 2008). The proposed numerical setup injects disperse gas bubbles with point mass sources close to the wall. A continuous injection of gas is also conceivable, but not investigated here because the focus is on porous plate injections, and the authors do not expect significant

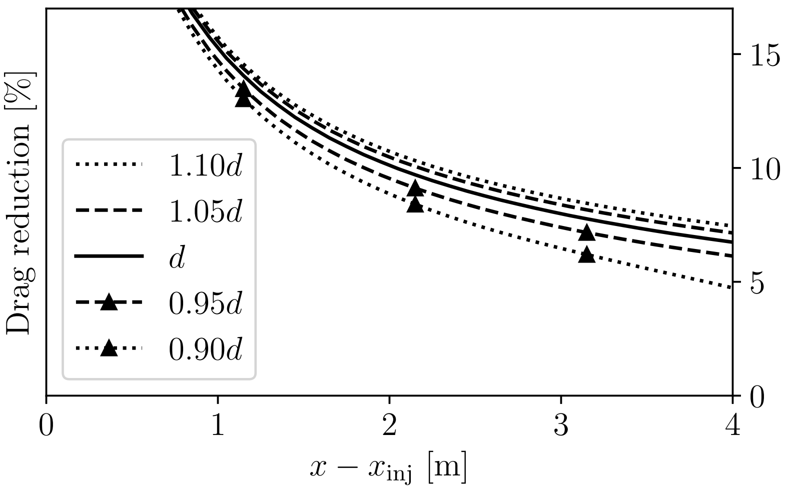

Fig. 5. The sensitivity of the simulation results with respect to the bubble diameter for the flat plate case was obtained for a free stream velocity of $U = 13.3\,\mathrm{m\,s^{-1}}$ and a gas flow rate of $q = 0.02\,\mathrm{m^2\,s^{-1}}$ (bubbly regime, zoom).

differences for the present setup. This can be concluded from Fig. 2, where continuous gas is formed right after the injection, but immediately disintegrated into disperse bubbles. An alternative numerical model for a gas injector is a patch inlet instead of a point mass source. This option may be relevant when modelling slot injectors with known inlet velocities. Such inlet velocities are usually unknown for porous plate injections, which is why point sources are the natural choice here (apart from more sophisticated models).

Bubble size. A discussion on the relevance of the bubble size can be found in Kato and Kodama (2003). Additional investigations with the current model show that the results for the drag reduction are robust against an increase in the bubble size, whereas a decrease may lead to larger deviations. An example is presented in Fig. 5 for a free stream velocity of $U = 13.3\,\mathrm{m\,s^{-1}}$ and a gas flow rate of $q = 0.02\,\mathrm{m^2\,s^{-1}}$. An increase and a decrease of the bubble diameter revealed that the results are robust against diameter variations of $\pm 5\%$. Even an increase of $+10\%$ did not significantly influence the results. However, a further decrease in the bubble size seems critical, and a deviation of -10% leads to significantly different results (Fig. 5). Future studies should investigate whether a polydisperse approach (such as the population balance model (Lehnigk et al., 2021)) is relevant for certain operating points.

Spatial resolution. Morphology-adaptive methods are sensitive to the local spatial resolution to optimally use a given mesh. A given structure is represented only as a continuous phase if the local resolution is sufficient. If the mesh is too coarse, the bubbles cannot turn into an air layer. The disperse morphology would then serve as a rough approximation of an air layer. For the presented case, the resolution was chosen to be sufficiently fine to allow air layers with a thickness of a few millimeters. A refinement with factor two in the vertical direction revealed no significant differences.

Diameter-cell size ratio. Another aspect is that the Euler-Euler closures may lead to unphysical results when the bubble diameter covers multiple cells (Tomiyama et al., 2003; Krull et al., 2024). In the simulations presented, this was not a problem, as the bubble diameter was small relative to the local cell size.

A more comprehensive sensitivity study of air lubrication predictions obtained using the proposed method can be found in Kringel et al. (2026).

4. Influence of free stream velocity and gas flow rate

The generic flat plate setup from the previous section was used for parameter studies to investigate the influence of the free stream velocity U and the gas flow rate q on the morphology (bubble dominance or air layer dominance) and the corresponding drag reduction. The free stream velocity U was varied according to $[6.7, 8.9, 11.1, 13.3]\,\mathrm{m\,s^{-1}}$ and the gas flow rate q was varied according to $[0, 0.02, 0.05, 0.08]\,\mathrm{m^2\,s^{-1}}$. This set of parameters was inspired by the settings investigated in Elbing et al. (2008).

4.1. Gas morphology

The gas morphology strongly depends on the combination of liquid velocity and gas flow rate. It is of interest how much gas remains in the vicinity of the hull and whether it stays bubbly or tends to form an air layer. The gas-holdup

$$\frac{V_{\mathrm{air}}}{V_{\mathrm{domain}}} \quad \text{with} \quad V_{\mathrm{air}} = V_{\mathrm{aird}} + V_{\mathrm{airc}}$$

expresses the amount of gas in the domain independent of its morphology. It is shown in Fig. 6. It is plausible that a higher free stream velocity requires a higher gas flow rate to achieve a certain gas holdup level.

To assess the morphology, the continuous fraction of gas was computed, indicating the existence of an air layer. Fig. 7 shows a clear line of transition from bubble-dominated to air layer dominated regimes. As discussed in Section 3.4, there is a sudden change from the bubble-dominated regime to the air-layer-dominated regime.

Note that knowledge of the integral gas volume is insufficient to predict the existence of an air layer: for a gas holdup of 0.7% for example, an air layer may or may not exist (compare the parameter pairs with a value 0.7% in Fig. 6 with the corresponding entries in Fig. 7 showing 0.6% and 93% for the continuous fraction). Overall, a clear trend was observed: both the gas holdup and air layer fraction benefit from high gas flow rates in combination with a low free stream velocity, at least in the parameter range investigated in this study.

4.2. Drag reduction

The objective of this section is to investigate the drag reduction induced by the morphologies reported in the previous section. The total

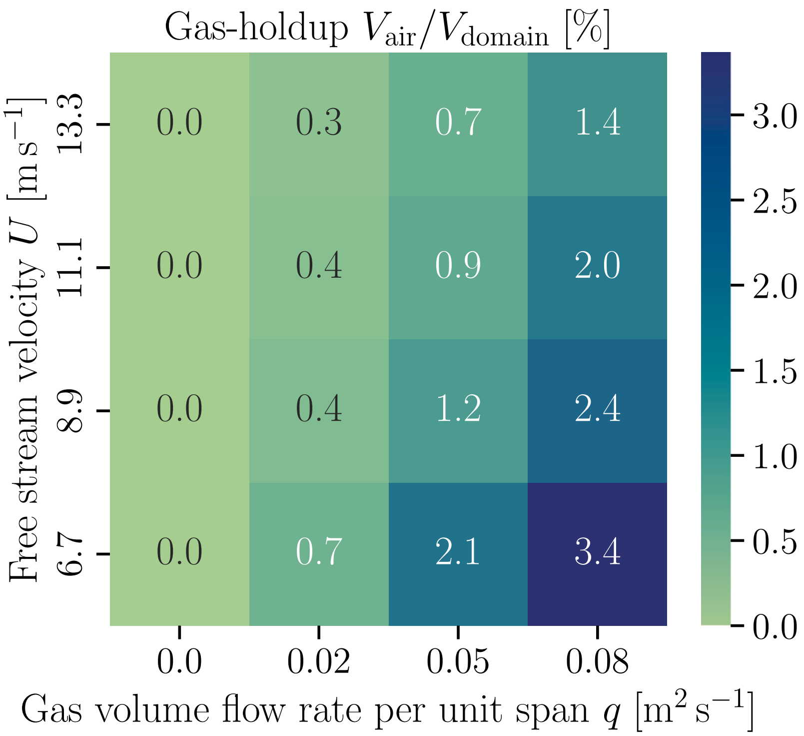

Fig. 6. Influence of free stream velocity and gas flow rate on gas-holdup.

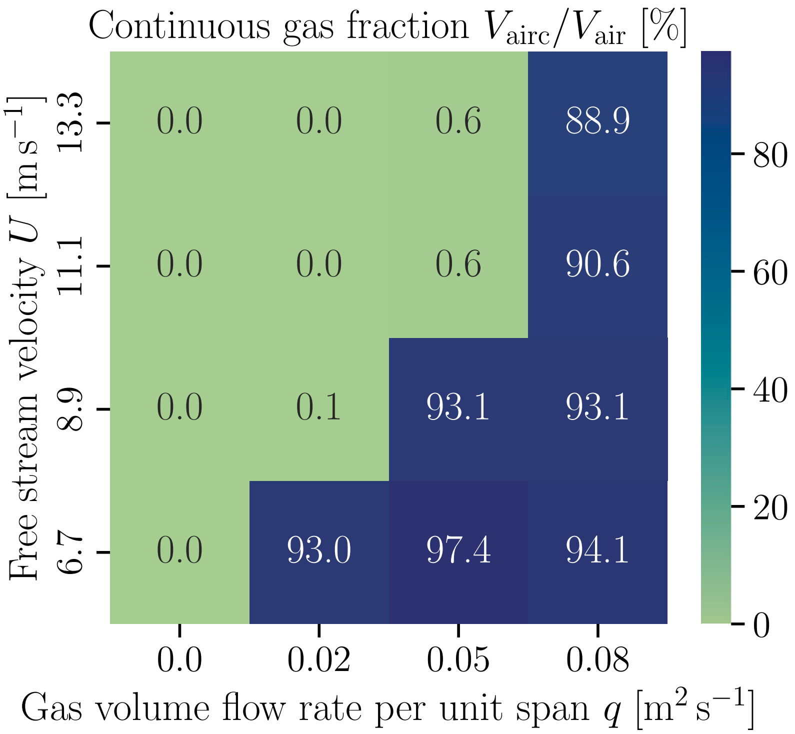

Fig. 7. Influence of free stream velocity and gas flow rate on the existence of air layers.

frictional drag per unit area was computed for the defined operation points by integrating the frictional stress along the wall, and is denoted by $\langle \tau_{\mathrm{w}} \rangle$. The results are shown in Fig. 8. As expected, the drag increased nonlinearly with the free stream velocity. Two additional variations of the same plot are provided to simplify the discussion: First, each result was normalized to the case with the result obtained for the same free stream velocity but without gas injection (Fig. 9). This reveals how gas flow rate variations affect the drag: quite low gas flow rates are sufficient to produce a significant drag reduction, even at higher free stream velocities (at least −9% for $q = 0.02\,\mathrm{m}^2\,\mathrm{s}^{-1}$). Provided that sufficient air is injected, the drag can be reduced to approximately 22% for all the given free stream velocities. Similar reduction rates are possible in the given velocity range. A second perspective on the same information was created by normalizing each result with the

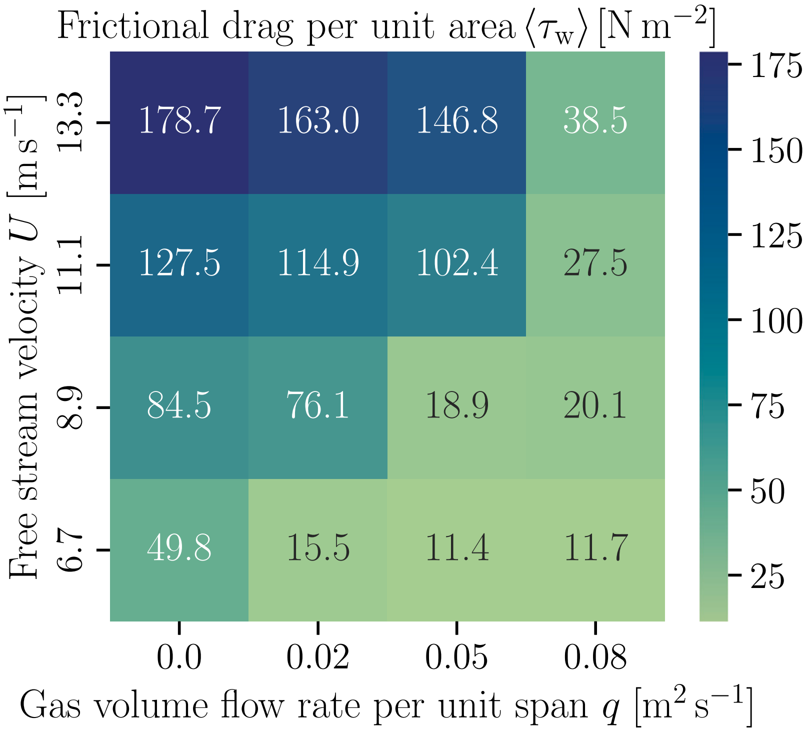

Fig. 8. Influence of free stream velocity and gas flow rate on total frictional resistance.

result obtained for the lowest free stream velocity with the same gas flow rate (Fig. 10). This reveals how a variation in the free stream velocity (ship velocity) affects drag. If there is sufficient gas injected, the drag growth is comparable to that in the single-phase situation (comparing the factors for $q = 0\,\mathrm{m^2\,s^{-1}}$ and $q = 0.08\,\mathrm{m^2\,s^{-1}}$ in Fig. 10). However, increasing the free stream (ship) velocity with a fixed gas flow rate bears the risk of losing the gas layer, causing a drag increase by more than a factor of ten (compare the factors for $q = 0.02\,\mathrm{m^2\,s^{-1}}$ and $q = 0.05\,\mathrm{m^2\,s^{-1}}$ in Fig. 10).

The parameter study confirmed that the presence of an air layer has a significant effect. As soon as an air layer is formed, further gas injection is no longer required. Dynamically controlling gas injection appears to be fundamentally important in practical applications to prevent sudden and multiple increases in drag.

5. Exemplary application to a ship hull geometry

The application of the MultiMorph model to a generic ship hull geometry is presented in this section. The operating conditions were chosen to meet one of the flat-plate experiments by Elbing et al. (2008), also covered in the parameter study presented in Section 4. Such a three-dimensional setup results in a significant increase in complexity: the geometry is curved, flow structures may vary in the spanwise direction, gas may escape laterally, and the importance of the turbulent dispersion may change due to a different turbulence level. The aim of this study is to demonstrate the applicability of this method. More effort is required to answer specific technical design questions.

5.1. Case description

The demonstration case is based on the publicly available DTC container ship geometry (Moctar et al., 2012) and reflects the operating conditions that are representative of sea vessels. The corresponding Froude number is Fr = 0.16. The case parameters are presented in Table 2, if not mentioned in the text. The ship hull is proportionally scaled to a length of L_{ship} and embedded in a fluid half-domain of length L with a half-width of W and a depth of D, which considers the draught of the ship (Fig. 11). There is an inlet and an outlet boundary condition, the no-slip condition is applied to the ship hull (slip allowed for bubbles), and the free-slip condition is applied to the top boundary to mimic the water surface. The remaining boundaries were defined as symmetry boundaries. In contrast to the generic flat plate setup, the fixed mean pressure outlet boundary condition is no longer required because there is no continuous air layer crossing the outlet. A homogeneous *Neumann* boundary condition is applied. The ship hull was at rest, and the free stream velocity (inlet velocity) was set to $U = 6.7\,\mathrm{m\,s^{-1}}$. The turbulence intensity I_0 was assumed to be significantly lower than that in the flat-plate case. The gas-injection rate was set to $q = 0.02\,\mathrm{m^2\,s^{-1}}$. The flat-plate investigations suggest that there is a good chance of obtaining an air layer for this operating point (Fig. 7). There are two lines where the gas is injected, one of length L_1 at position x_1 and another of length L_2 at position x_2 (see Fig. 11). They are realized as rows of equidistant mass source points, located 1 cm below the hull, distributed equidistantly, with a distance of 25 cm. The bubbles were assumed to be monodisperse with diameter d_{b}, keeping the value from the flat-plate simulations. A wall-normal cell thickness of 2 mm was imposed close to the ship hull, resulting in the number of cells reported in Table 2. The time step was adjusted to ensure a maximum global Courant number of 0.4. The setup is publicly available (Hänsch et al., 2024).

Table 2
Setup parameters for the ship hull case.

L	W	D	L_{ship}	x_1, L_1	x_2, L_2	d_b	I_0	N_{cells}
300 m	100 m	157.3 m	180 m	120 m, 12 m	90 m, 14 m	0.3 mm	0.1%	125,059

5.2. Results

The results of the ship hull simulation are presented. A snapshot of a typical situation is shown in Fig. 12. A magnified view of this situation is shown in Fig. 13. The injectors are indicated by black lines. The presence of disperse gas was visualized with two isosurfaces: one

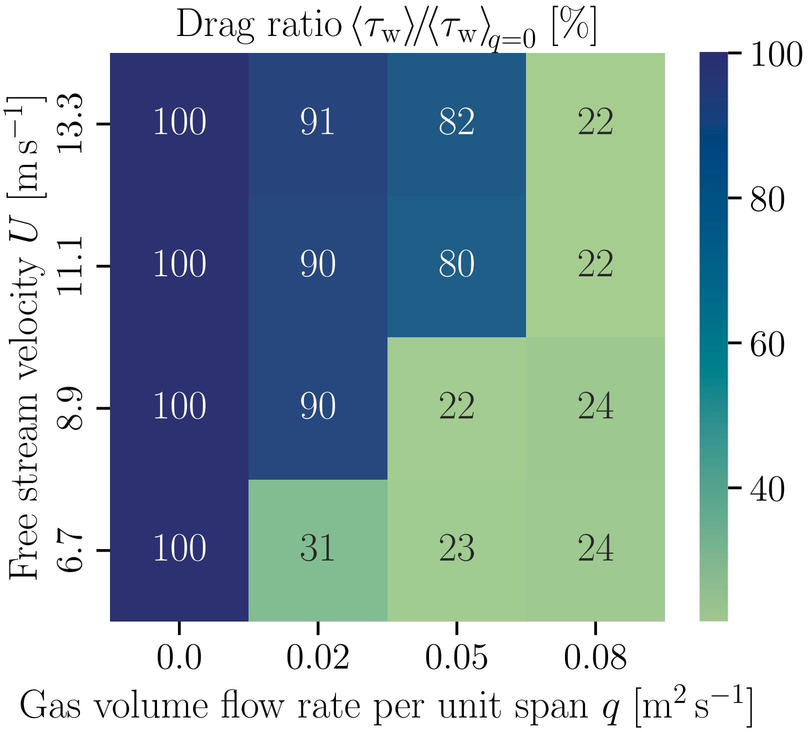

Fig. 9. Same data as in Fig. 8, normalized to investigate the effect of changing the gas flow rates when the free stream velocity is kept constant. Each line is normalized with the corresponding drag value obtained for the single-phase situation without gas injection (read plot line-by-line).

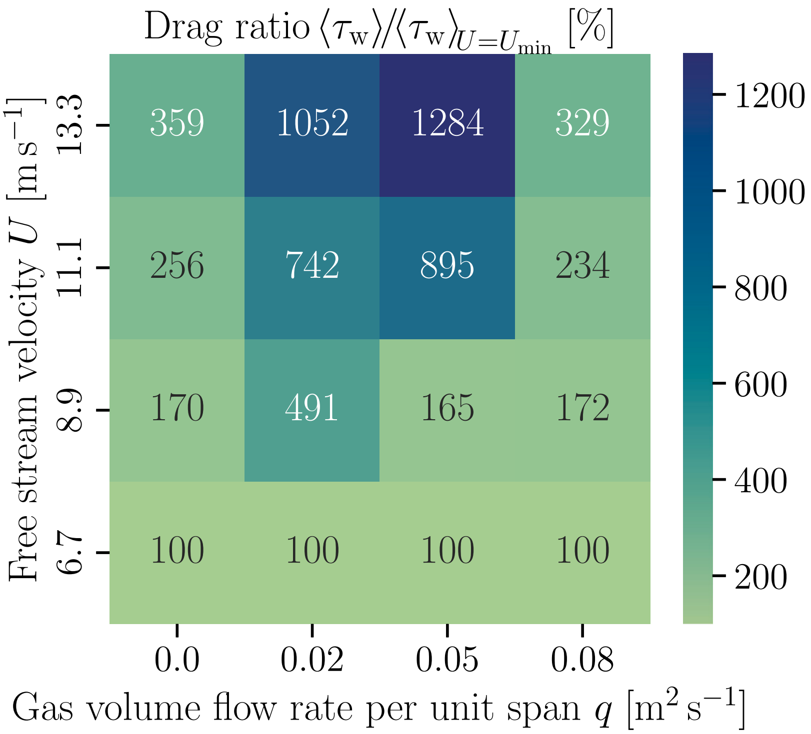

Fig. 10. Same data as in Fig. 8, normalized to investigate the effect of changing the free stream velocities when the gas flow rate was kept constant. Each column was normalized with the corresponding drag value obtained for the lowest velocity under consideration (read plot column-by-column).

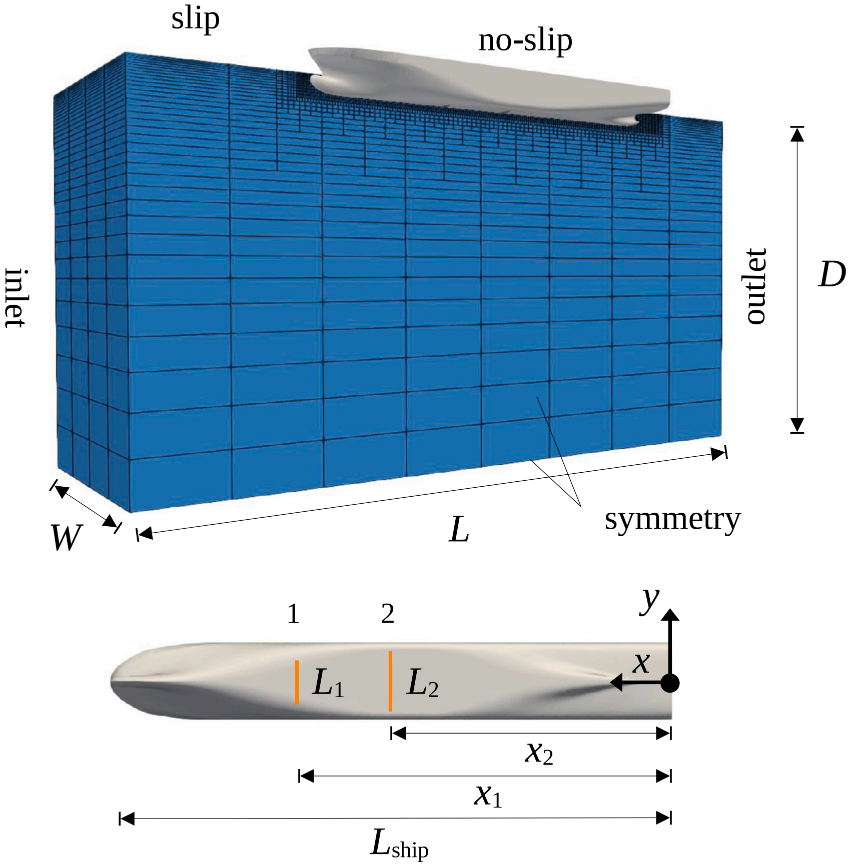

Fig. 11. Sketch of the computational domain together with the ship geometry (top) and sketch of position and length of the injectors (bottom).

isosurface for $\alpha_\text{aird} = 0.005$ (transparent) and one for $\alpha_\text{aird} = 0.05$ (less transparent). The continuous gas distribution was visualized with an isosurface for $\alpha_\text{airc} = 0.5$. The ratio between the computational time and simulation time was approximately 190, obtained using eight cores, which means that approximately three hours computational time is required to compute a physical minute. It should be noted that the computational effort strongly depends on the refinement level close to the wall.

It can be seen in Fig. 12 that some regions are dominated by bubbles (orange) and others are dominated by air layers (blue). In particular, the region downstream of the first injector was inhomogeneous, revealing a transitional regime. The gas structures in this area were highly unsteady. Downstream from the second injector, sufficient gas was available to form a continuous air layer. This layer remained stable and oscillated slightly, primarily in the longitudinal direction. Further downstream, the air layer disintegrates back into bubbles, leaving the hull. Some bubbles escaped laterally at low concentrations (Fig. 13), partially enclosed in a trailing vortex detached from the hull (the transparent structure in Fig. 12).

The gas structures directly influence the local frictional stress. A snapshot of the instant distribution of drag reduction is shown in Fig. 14. The single-phase reference was computed using the same configuration with zero gas flow rate. The frictional resistance in the front region remained unaffected, and there was no significant change upstream of the injectors. The local morphology of the gas is shown in Fig. 15. Between the injectors, in the mixed regime, the drag reduction varies significantly because of the instantaneous wavy gas structures. Similar structures have been observed experimentally under different operating conditions (Tanaka et al., 2020). Downstream of the second injector, the drag decreased significantly owing to the formation of a stable air layer. These conditions are ideal with regard to drag reduction. However, an increase in the frictional resistance is predicted in the rear section of the hull after the air layer has disintegrated into bubbles. The local increase in the frictional shear can be visualized by the negative iso-surfaces of the Q criterion (Chen et al., 2015), as shown in Fig. 16.

These three-dimensional high-shear regions were not observed in the single-phase case and appeared with relatively high bubble concentrations (compare Fig. 16 with Fig. 15). The method reveals the complex interplay between gas morphologies (bubbles, air layer, air layer formation, and air layer disintegration) and the flow field (significantly modified), both of which directly influence the local frictional resistance on the hull. The results suggest that operating conditions with an early smooth lateral drain of gas could be beneficial for the integral air lubrication efficiency. The proposed method allows specific design goals to be addressed as it allows the testing of different injector arrangements and operating conditions.

6. Conclusions and perspectives

The MultiMorph model has been proven to be capable of predicting the phenomenon of air lubrication, covering both bubbly and air layer regimes, including the transition between them. The proposed method was successfully validated against flat-plate experiments. The same setup was used to study the influence of the water velocity and gas flow rate combinations on gas morphology and drag reduction. The model was applied to a full ship hull geometry using two gas injectors. The gas morphologies in this exemplary case vary strongly, with a direct impact

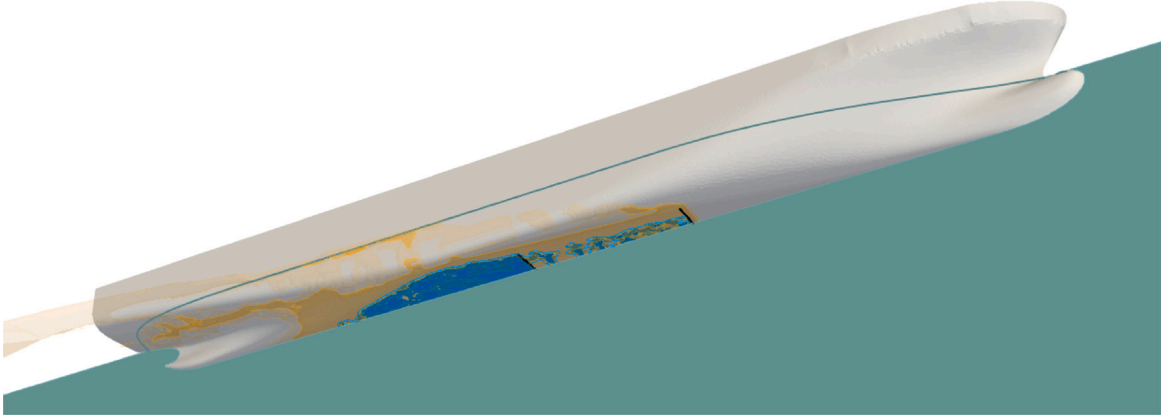

Fig. 12. Snapshot of gas morphologies. Bubbles are visualized by isosurfaces for the disperse gas (strong orange: $\alpha_{\mathrm{aird}} = 0.05$; light orange: $\alpha_{\mathrm{aird}} = 0.005$), and air layers are visualized by isosurfaces for the continuous gas (blue, $\alpha_{\mathrm{airc}} = 0.5$). Disperse gas is injected along the black lines.

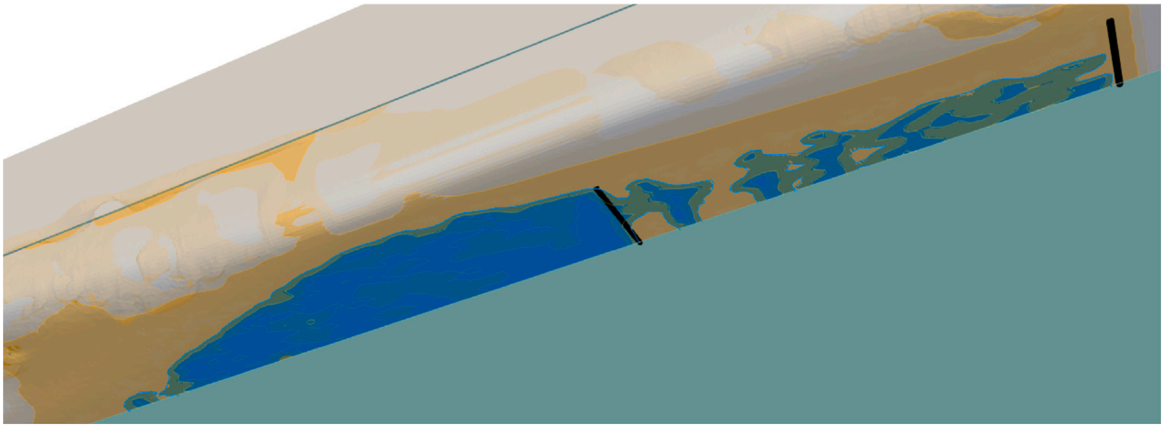

Fig. 13. Zoom of Fig. 12.

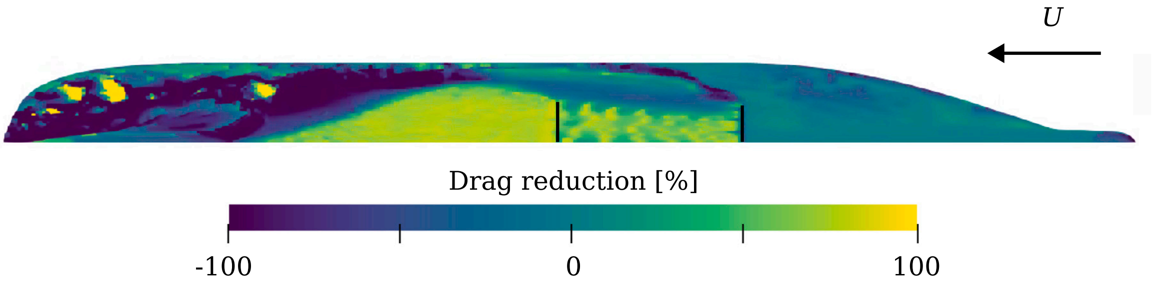

Fig. 14. Snapshot of the local drag reduction ($t = 300\,\mathrm{s}$, clipped at $\pm 100\%$).

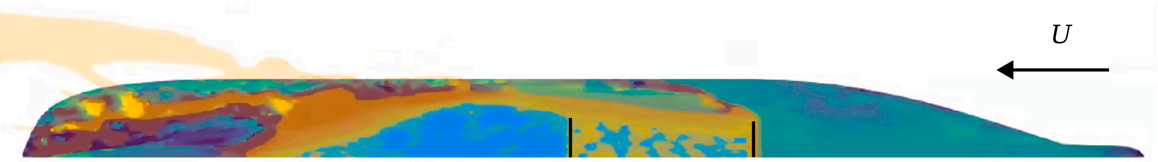

Fig. 15. Local drag reduction (same as in Fig. 14), complemented by volume fraction iso-surfaces visualizing the local gas morphology (strong orange: high bubble concentration, $\alpha_{\mathrm{aird}} = 0.05$; light orange: low bubble concentration, $\alpha_{\mathrm{aird}} = 0.005$; blue: air layer, $\alpha_{\mathrm{airc}} = 0.5$).

on local friction. In particular, the flow in the rear area appeared to be significantly more complex than that without gas injection.

The MultiMorph method has been qualified for further numerical investigations of ship hull air lubrication systems, addressing specific design optimizations. It can also be applied in cases where the free stream velocity and gas rate are time-dependent, as the gas morphology adapts dynamically. The method is sufficiently efficient to perform rapid two-dimensional parameter studies within a few hours or a three-dimensional simulation in less than a day, at least for the parameters considered here. The unique ability of this method to capture different

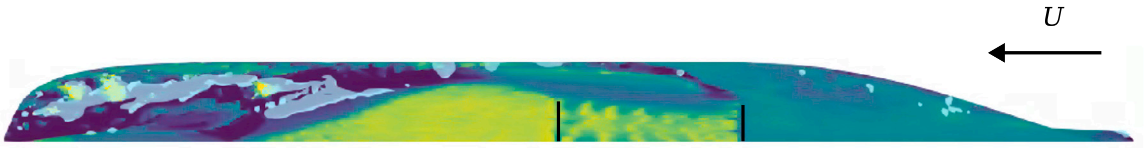

Fig. 16. Local drag reduction (same as in Fig. 14), complemented by a visualization of local shear structures (Q criterion iso-surface for $Q = -1$, light blue).

morphologies, including the transition, has proven to be advantageous for the study of large-scale problems with air lubrication.

Future investigations could focus on different ship hull geometries, the variation of injector designs (arrangement, oscillating injectors, coupled out-of-phase injectors, slot injectors), the impact of transient gas patterns, minimization of lateral gas escape, the gas distribution in the propeller region, the influence of hull shape irregularities (wall roughness or typical deformations of large vessels), or the influence of varying draughts and trim angles.

Depending on the design question of interest, the model can be assessed or extended according to the following aspects: importance of modelling the free water surface allowing waves and the escape of gas to the atmosphere, validity of interfacial closures for bubbly flows in sea water, relevance of bubble coalescence and breakup for sea water, existence and influence of slugs and wavy gas structures. A film model could be a useful extension of the model, potentially allowing a reduction in computational effort. This must be realized so that more complex structures are not suppressed: the film morphology should be allowed to exist without prescribing its existence. Film formation and stability are the crucial aspects of this process. A comparison with model experiments should be performed to identify the next modelling steps.

CRediT authorship contribution statement

Benjamin Krull: Writing – review & editing, Writing – original draft, Visualization, Validation, Supervision, Software, Methodology, Investigation, Formal analysis, Data curation, Conceptualization. **Kasper Bilde:** Writing – review & editing, Validation, Supervision, Project administration, Methodology, Investigation, Data curation, Conceptualization. **Christian Kringel:** Writing – review & editing, Validation, Investigation, Data curation, Conceptualization. **Richard Meller:** Writing – review & editing, Visualization, Validation, Software, Methodology, Investigation, Data curation, Conceptualization. **Victor Molbak:** Validation, Investigation, Conceptualization. **Georgios Papaioannou:** Writing – review & editing, Validation, Project administration, Investigation, Formal analysis, Conceptualization. **Fabian Schlegel:** Writing – review & editing, Supervision, Software, Project administration, Methodology, Investigation, Funding acquisition, Conceptualization. **Matej Tekavčič:** Writing – review & editing, Validation, Software, Methodology, Investigation, Funding acquisition, Conceptualization. **Filotas Tziaros:** Writing – review & editing, Investigation, Conceptualization.

Declaration of competing interest

The authors declare that they have no known competing financial interests or personal relationships that could have appeared to influence the work reported in this paper.

Acknowledgements

The author from the Jožef Stefan Institute gratefully acknowledges the financial support provided by the Slovenian Research and Innovation Agency through Grant P2-0026.

References

An, H., Pan, H., Yang, P., 2022. Research progress of air lubrication drag reduction technology for ships. Fluids (ISSN: 2311-5521) 7 (10), 319. http://dx.doi.org/10.3390/fluids7100319.

Brackbill, J., Kothe, D., Zemach, C., 1992. A continuum method for modeling surface tension. J. Comput. Phys. 100 (2), 335–354. http://dx.doi.org/10.1016/0021-9991(92)90240-y.

Burns, A., Frank, T., Hamill, I., Shi, J.-M., 2004. The favre averaged drag model for turbulent dispersion in Eulerian multi-phase flows. In: 5th International Conference on Multiphase Flow, ICMF'04, Yokohama, Japan, May 30-June 4, 2004, Paper No. 392.

Ceccio, S.L., 2010. Friction drag reduction of external flows with bubble and gas injection. Annu. Rev. Fluid Mech. 42, 183.

Chen, Q., Zhong, Q., Qi, M., Wang, X., 2015. Comparison of vortex identification criteria for planar velocity fields in wall turbulence. Phys. Fluids (ISSN: 1089-7666) 27 (8), http://dx.doi.org/10.1063/1.4927647.

Chillemi, M., Raffaele, M., Sfravara, F., 2024. A review of advanced air lubrication strategies for resistance reduction in the naval sector. Appl. Sci. (ISSN: 2076-3417) 14 (13), 5888. http://dx.doi.org/10.3390/app14135888.

Elbing, B.R., Mäkiharju, S., Wiggins, A., Perlin, M., Dowling, D.R., Ceccio, S.L., 2013. On the scaling of air layer drag reduction. J. Fluid Mech. (ISSN: 1469-7645) 717, 484–513. http://dx.doi.org/10.1017/jfm.2012.588.

Elbing, B.R., Winkel, E.S., Lay, K.A., Ceccio, S.L., Dowling, D.R., Perlin, M., 2008. Bubble-induced skin-friction drag reduction and the abrupt transition to air-layer drag reduction. J. Fluid Mech. 612, 201–236. http://dx.doi.org/10.1017/s0022112008003029.

Fotopoulos, A.G., Margaris, D.P., 2020. Computational analysis of air lubrication system for commercial shipping and impacts on fuel consumption. Computation (ISSN: 2079-3197) 8 (2), 38. http://dx.doi.org/10.3390/computation8020038.

Giernalczyk, M., Kaminski, P., 2021. Assessment of the propulsion system operation of the ships equipped with the air lubrication system. Sensors (ISSN: 1424-8220) 21 (4), 1357. http://dx.doi.org/10.3390/s21041357.

Guin, M.M., Kato, H., Yamaguchi, H., Maeda, M., Miyanaga, M., 1996. Reduction of skin friction by microbubbles and its relation with near-wall bubble concentration in a channel. J. Mar. Sci. Technol. 1 (5), 241–254. http://dx.doi.org/10.1007/bf02390723.

Hänsch, S., Draw, M., Evdokimov, I., Khan, H., Kamble, V.V., Krull, B., Lehnigk, R., Liao, Y., Lyu, H., Meller, R., Schlegel, F., Tekavčič, M., 2024. Multiphase Cases Repository by HZDR for OpenFOAM Foundation Software. http://dx.doi.org/10.14278/rodare.2322, URL https://rodare.hzdr.de/record/811.

Hänsch, S., Evdokimov, I., Schlegel, F., Lucas, D., 2021. A workflow for the sustainable development of closure models for bubbly flows. Chem. Eng. Sci. 244, 116807. http://dx.doi.org/10.1016/j.ces.2021.116807.

Jang, J., Choi, S.H., Ahn, S.-M., Kim, B., Seo, J.S., 2014. Experimental investigation of frictional resistance reduction with air layer on the hull bottom of a ship. Int. J. Nav. Archit. Ocean. Eng. (ISSN: 2092-6782) 6 (2), 363–379. http://dx.doi.org/10.2478/ijnaoe-2013-0185.

Kato, H., Kodama, Y., 2003. Microbubbles as a skin friction reduction device–a midterm review of the research. In: Proceedings of the 4th Symposium on Smart Control of Turbulence, Tokyo, Japan. pp. 2–4.

Kato, H., Miura, K., Yamaguchi, H., Miyanaga, M., 1998. Experimental study on microbubble ejection method for frictional drag reduction. J. Mar. Sci. Technol. (ISSN: 1437-8213) 3 (3), 122–129. http://dx.doi.org/10.1007/bf02492919.

Kim, D.-Y., Ha, J.-Y., Paik, K.-J., 2020. Numerical study on the extrapolation method for predicting the full-scale resistance of a ship with an air lubrication system. J. Ocean. Eng. Technol. (ISSN: 2287-6715) 34 (6), 387–393. http://dx.doi.org/10.26748/ksoe.2020.008.

Kim, H., Park, S., 2021. Coupled level-set and volume of fluid (CLSVOF) solver for air lubrication method of a flat plate. J. Mar. Sci. Eng. (ISSN: 2077-1312) 9 (2), 231. http://dx.doi.org/10.3390/jmse9020231.

Kringel, C., Simonsen, A.S., Hærvig, J., 2026. Parameter sensitivity study of a morphology-adaptive CFD model for flat plate air lubrication. Ocean Eng. (ISSN: 0029-8018) 343, 123438. http://dx.doi.org/10.1016/j.oceaneng.2025.123438.

Krull, B., Meller, R., Tekavčič, M., Schlegel, F., 2024. A filtering approach for applying the two-fluid model to gas-liquid flows on high resolution grids. Chem. Eng. Sci. (ISSN: 0009-2509) 119909. http://dx.doi.org/10.1016/j.ces.2024.119909.

Kunz, R.F., Gibeling, H.J., Maxey, M.R., Tryggvason, G., Fontaine, A.A., Petrie, H.L., Ceccio, S.L., 2006. Validation of two-fluid Eulerian CFD modeling for microbubble drag reduction across a wide range of Reynolds numbers. J. Fluids Eng. (ISSN: 1528-901X) 129 (1), 66–79. http://dx.doi.org/10.1115/1.2375124.

Legner, H.H., 1984. A simple model for gas bubble drag reduction. Phys. Fluids (ISSN: 0031-9171) 27 (12), 2788–2790. http://dx.doi.org/10.1063/1.864592.

Lehnigk, R., Bainbridge, W., Liao, Y., Lucas, D., Niemi, T., Peltola, J., Schlegel, F., 2021. An open-source population balance modeling framework for the simulation of polydisperse multiphase flows. AIChE J. 68 (3), http://dx.doi.org/10.1002/aic.17539.

Lehnigk, R., Bruschewski, M., Huste, T., Lucas, D., Rehm, M., Schlegel, F., 2023. Sustainable development of simulation setups and addons for OpenFOAM for nuclear reactor safety research. Kerntechnik 88 (2), 131–140. http://dx.doi.org/10.1515/kern-2022-0107.

Ma, T., Santarelli, C., Ziegenhein, T., Lucas, D., Fröhlich, J., 2017. Direct numerical simulation–based Reynolds-averaged closure for bubble-induced turbulence. Phys. Rev. Fluids (ISSN: 2469-990X) 2 (3), http://dx.doi.org/10.1103/PhysRevFluids.2.034301.

Mäkiharju, S.A., Perlin, M., Ceccio, S.L., 2012. On the energy economics of air lubrication drag reduction. Int. J. Nav. Archit. Ocean. Eng. (ISSN: 2092-6782) 4 (4), 412–422. http://dx.doi.org/10.2478/ijnaoe-2013-0107.

Meller, R., Krull, B., Schlegel, F., Tekavčič, M., 2024. Numerical transfer towards unresolved morphology representation in the MultiMorph model. Nucl. Eng. Des. 428, 113470, 1–11. http://dx.doi.org/10.1016/j.nucengdes.2024.113470, URL https://www.sciencedirect.com/science/article/pii/S0029549324005703.

Meller, R., Schlegel, F., Lucas, D., 2021. Basic verification of a numerical framework applied to a morphology adaptive multifield two-fluid model considering bubble motions. Internat. J. Numer. Methods Fluids 93 (3), 748–773. http://dx.doi.org/10.1002/fld.4907.

Menter, F.R., 2009. Review of the shear-stress transport turbulence model experience from an industrial perspective. Int. J. Comput. Fluid Dyn. 23, 305–316.

Mizokami, S., Kawakita, C., Kodan, Y., Takano, S., Higasa, S., Shigenaga, R., 2010. Experimental study of air lubrication method and verification of effects on actual hull by means of sea trial. Mitsubishi Heavy Ind. Tech. Rev. 47 (3), 41–47.

Moctar, O.e., Shigunov, V., Zorn, T., 2012. Duisburg test case: Post-panamax container ship for benchmarking. Ship Technol. Res. (ISSN: 2056-7111) 59 (3), 50–64. http://dx.doi.org/10.1179/str.2012.59.3.004.

Mohanarangam, K., Cheung, S., Tu, J., Chen, L., 2009. Numerical simulation of micro-bubble drag reduction using population balance model. Ocean Eng. (ISSN: 0029-8018) 36 (11), 863–872. http://dx.doi.org/10.1016/j.oceaneng.2009.05.001.

Murai, Y., 2014. Frictional drag reduction by bubble injection. Exp. Fluids (ISSN: 1432-1114) 55 (7), http://dx.doi.org/10.1007/s00348-014-1773-x.

Park, S.H., Lee, I., 2018. Optimization of drag reduction effect of air lubrication for a tanker model. Int. J. Nav. Archit. Ocean. Eng. (ISSN: 2092-6782) 10 (4), 427–438. http://dx.doi.org/10.1016/j.ijnaoe.2017.09.003.

Qin, S., Chu, N., Yao, Y., Liu, J., Huang, B., Wu, D., 2017. Stream-wise distribution of skin-friction drag reduction on a flat plate with bubble injection. Phys. Fluids (ISSN: 1089-7666) 29 (3), http://dx.doi.org/10.1063/1.4977800.

Rzehak, R., Kriebitzsch, S., 2015. Multiphase CFD-simulation of bubbly pipe flow: A code comparison. Int. J. Multiph. Flow 68, 135–152.

Schlegel, F., Bilde, K.G., Draw, M., Evdokimov, I., Hänsch, S., Kamble, V.V., Khan, H., Krull, B., Lehnigk, R., Li, J., Lyu, H., Meller, R., Petelin, G., Kota, S.P., Tekavcic, M., 2024. Multiphase Code Repository by HZDR for OpenFOAM Foundation software. http://dx.doi.org/10.14278/rodare.767, URL https://rodare.hzdr.de/record/767.

Schlegel, F., Meller, R., Krull, B., Lehnigk, R., Tekavčič, M., 2023. OpenFOAM-Hybrid: A morphology adaptive multifield two-fluid model. Nucl. Sci. Eng. 197 (10), 2620–2633. http://dx.doi.org/10.1080/00295639.2022.2120316, Selected papers from the 19th International Topical Meeting on Nuclear Reactor Thermal Hydraulics (NURETH-19).

Strubelj, L., Tiselj, I., 2011. Two-fluid model with interface sharpening. Internat. J. Numer. Methods Engrg. 85, 575–590. http://dx.doi.org/10.1002/nme.2978.

Tanaka, T., Park, H.J., Tasaka, Y., Murai, Y., 2020. Spontaneous and artificial void wave propagation beneath a flat-bottom model ship. Ocean Eng. (ISSN: 0029-8018) 214, 107850. http://dx.doi.org/10.1016/j.oceaneng.2020.107850.

Tekavčič, M., Meller, R., Schlegel, F., 2021. Validation of a morphology adaptive multifield two-fluid model considering counter-current stratified flow with interfacial turbulence damping. Nucl. Eng. Des. 379, 111223. http://dx.doi.org/10.1016/j.nucengdes.2021.111223.

Thill, C., Toxopeus, S., van Walree, F., 2005. Project energy-saving air-lubricated ships (PELS). In: Proceedings of the 2nd International Symposium on Seawater Drag Reduction. pp. 1–16.

Tomiyama, A., Shimada, N., Asano, H., 2003. Application of number density transport equation for the recovery of consistency in multi-field model. In: Proceedings of ASME FEDSM'03, 4th ASME_JSME Joint Fluids Engineering Conference Honolulu, Hawaii, USA, July 6-10, 2003. Honolulu, Hawaii, USA.

Wang, L.-S., Krull, B., Lucas, D., Meller, R., Schlegel, F., Tekavčič, M., Xu, J.-Y., 2023. Simulation of droplet entrainment in annular flow with a morphology adaptive multifield two-fluid model. Phys. Fluids 35 (10), http://dx.doi.org/10.1063/5.0169288.

Wang, H., Wang, K., Liu, G., 2022. Drag reduction by gas lubrication with bubbles. Ocean Eng. (ISSN: 0029-8018) 258, 111833. http://dx.doi.org/10.1016/j.oceaneng.2022.111833.

Wiedemann, P., Meller, R., Schubert, M., Hampel, U., 2023. Application of a hybrid multiphase CFD approach to the simulation of gas–liquid flow at a trapezoid fixed valve for distillation trays. Chem. Eng. Res. Des. 193, 777–786. http://dx.doi.org/10.1016/j.cherd.2023.04.016.

Yin, J., Zhang, T., Krull, B., Meller, R., Schlegel, F., Lucas, D., Wang, D., Liao, Y., 2023. A CFD approach for the flow regime transition in a vane-type gas-liquid separator. Int. J. Multiph. Flow 159, 104320. http://dx.doi.org/10.1016/j.ijmultiphaseflow.2022.104320.

Zhao, X., Zong, Z., Jiang, Y., Sun, T., 2020. A numerical investigation of the mechanism of air-injection drag reduction. Appl. Ocean Res. (ISSN: 0141-1187) 94, 101978. http://dx.doi.org/10.1016/j.apor.2019.101978.